MOF derived graphitic carbon nitride/oxygen vacancies-rich zinc oxide nanocomposites with enhanced supercapacitive performance

Jiaqi Shen[1], Peng Wang,[1] Huasheng Jiang[1], Hui Wang,[2] Bruno G. Pollet[3], Rongfang Wang[2], Shan Ji[1*]*

[1] College of Biological, Chemical Science and Chemical Engineering, Jiaxing University, Jiaxing, 314001, China

[2] State Key Laboratory Base for Eco-Chemical Engineering, College of Chemical Engineering, Qingdao University of Science and Technology, Qingdao, 266042, China

[3] Department of Energy and Process Engineering, Faculty of Engineering, Norwegian University of Science and Technology (NTNU) NO-7491 Trondheim, Norway

Abstract

Supercapacitors with high power density and durability have shown enormous potential for smart electronics. Herein, a novel graphitic carbon nitride (g-C_3N_4) coated with oxygen vacancies-rich ZnO (OZCN) nanocomposites were prepared from zeolitic imidazolate framework precursor by direct thermal decomposition melamine in air. The *as*-prepared OZCN nanocomposites exhibited high capacitive performance (3,528 $F.g^{-1}$ at 1$A.g^{-1}$) and excellent cycling stability due to the synergetic effect of g-C_3N_4 and oxygen vacancies-rich ZnO. Additionally, the assembled asymmetric supercapacitor displayed an energy density of 100.9 $Wh.kg^{-1}$, whilst the capacitance retention remained at 86.2% even after 1,000 cycles at 7 $A.g^{-1}$. This study is highlighting a new way for designing metal oxide electrode possessing excellent electronic properties for durable and low-cost energy storage devices.

Keywords: Energy storage; supercapacitor; ZIF-8; graphitic carbon nitride; zinc oxide

1. Introduction

With the development of portable electronic devices and hybrid electric vehicles, currently commercial large-capacity and fast-charging energy storage devices cannot satisfy consumer´s demands[1-3]. Supercapacitors, as energy electrochemical storage devices, are attracting widespread attention due to their various advantages, such as excellent power density, high efficiency, and superior cycling stability[4-6].

Zinc oxide (ZnO) nanomaterials are regarded as a promising candidate material for supercapacitors[7-9], due to their high energy density (ca. 650 $A.g^{-1}$), low cost, chemical stability and environmental friendliness. ZnO nanomaterials show distinctive spatial structures and high effective surface areas, which can meet some specific requirements in supercapacitor applications[10-11]. Unfortunately, the low rate capability and the poor reusability of ZnO materials seriously limit their practical applications, which is attributed to the slow *Faraday* redox kinetics and low electron transport capability[12-13]. Generally, these limitations can be overcome by using various nanocomposites made of carbon materials and transition metal oxides[14]. However, the surface/interface state and the poor crystallinity of the transition metal oxides in these nanocomposites can lead to poor electrical transmission properties of hybrid nanomaterials[15-17]. Therefore, novel nanomaterial design strategies are urgently required to overcome the current challenging obstacles.

Very recently, generating inherent defects in ZnO to change the electronic properties has gradually become an active research area. This is performed by controllably introducing inherent defects, for example, by creating oxygen vacancies into the metal oxide to adjust the materials´ densities and band structures, thereby controlling its electrical properties[18-20]. Many theoretical and experimental studies have shown that

various physical and chemical properties of ZnO, including electronic structure, charge transport and surface properties, are closely related to oxygen vacancies (Vo)[21-22]. For example, the appropriate Vo content in ZnO should help towards charge/carrier diffusion, resulting in better conductivity and higher capacitance when compared to "ideal" crystalline ZnO. Surface Vo should provide better OH^- adsorption (KOH as the electrolyte) and Vo could serve as the active site for the redox reactions and thus could accelerate surface reactions kinetics[23-25]. However, there are a few reports studying the combination of oxygen vacancies-rich ZnO with carbon materials together with a lack of effective design strategies.

Among various carbon materials, such as graphitic carbon nitride (g-C_3N_4), a sheet-like crystallite, has attracted a lot of research interest due to its excellent chemical and thermal stability, unique electronic characteristics, and simple synthesis process. Benefiting from its unique layered structure, charges are easily transferred in the horizontal direction[26-29]. Moreover, the high nitrogen (N) content in g-C_3N_4 can provide an active site for *Faraday* reactions, which can increase the surface polarity, improve the wettability of the electrode, and thus improve the electronic transmission efficiency[30-31]. More importantly, g-C_3N_4 acting as a soft polymer can be easily grafted and mixed with other materials[32-33], therefore the combination of g-C_3N_4 and oxygen vacancies-rich ZnO should yield interesting material properties.

Herein, a novel g-C_3N_4 coated oxygen vacancies-rich ZnO (OZCN) nanocomposites were successfully synthesized in a simple two-step reaction. g-C_3N_4 nanosheets were grafted onto the surface of OZCN and fully characterized by using various physical and electrochemical techniques. It was found that the Vo content of ZnO in OZCN was as high as 50.93%. Compared to reported ZnO/g-C_3N_4 composites[34-35], the OZCN electrode materials exhibited superior specific capacitance, reaching 3,528 $F.g^{-1}$ at 1

$A.g^{-1}$, and excellent cycling ability, up to 95.6% specific capacitance retention after 1,000 cycles. An asymmetric supercapacitor cell (ASC) was assembled by employing optimized OZCN as a positive electrode and activated carbon (AC) as a negative electrode, which led to very good capacitance (840 $F.g^{-1}$ at 1 $A.g^{-1}$), high power density and energy density (100.9 $Wh.kg^{-1}$), due to the synergy of g-C_3N_4 and oxygen vacancies-rich ZnO. This study highlights a facile method to produce transition metal-based electrode materials as efficient supercapacitor electrodes.

2. Experimental Section

2.1 Materials

In this study, analytical grade chemicals were used without any further purification. $Zn(CH_3COO)_2 \cdot 2H_2O$, 2-methylimidazole, hexadecyl trimethyl ammonium bromide, cetyltrimethylammonium bromide (CTAB), melamine, and ethanol were purchased from Alfa Aesar.

2.2 Synthesis of truncated rhombic dodecahedral zeolitic imidazolate framework-8 (TRD-ZIF-8) nanoparticles

In a typical synthesis[36], $Zn(CH_3COO)_2 \cdot 2H_2O$ (600 mg) dissolved in 10 mL of water was added to varying quantities of 2-methylimidazole (0.54 mM) and CTAB (2.58 mM) dissolved in 10 mL of water with gentle stirring for a few seconds. The resulting transparent mixture turned white after ca. 20 s and was left undisturbed at room temperature for 3 hours. The resulting TRD-ZIF-8 nanoparticles were washed three times with deionized water upon centrifugation at 9,000 rpm in 50 mL Falcon tubes. The collected wet pellets were then transferred in a vacuum drying box at 60 ^oC overnight to obtain the white powder TRD-ZIF-8 nanoparticles.

2.3 Synthesis of oxygen vacancies-rich ZnO/g-C_3N_4 (OZCN) nanocomposites

The obtained TRD-ZIF-8 (2 g) nanoparticles and melamine (2 g) were mixed by using a vortex oscillator for 5-10 min, and then transferred into a 100 mL alumina crucible with a lid. The crucible was then placed into a muffle furnace. The temperature was set at a rate of 3 ^oC / min to 550 ^oC under air condition and then maintained at this temperature for 3 hours. After natural cooling down to room temperature, a yellowish powder OZCN was obtained.

2.3 Synthesis of oxygen vacancies-rich ZnO (OZ) nanocomposites

For comparison purposes, oxygen vacancies-rich ZnO (OZ) without g-C_3N_4 were

synthesized. In this case, the preparation method was the same as the one for OZCN, with the exception that melamine was not added before calcination process.

2.4 Physical Characterisation

IR spectra of KBr disks containing the samples were recorded using a Nicolet-360 FT-IR spectrometer and X-ray diffraction (XRD) measurements were obtained on a Rigaku CCD diffractometer with a Ni-filtered Cu(K_α) radiation (40 kV, 40 mA). Raman spectra were recorded on a Thermo Nicolet Almega XR Raman Microscope and powder X-ray diffraction (PXRD) data were collected on a D2 PHASER desk diffractometer from Bruker using Cu(K_α) radiation generated at 30 kV and 10 mA. X-ray Photoelectron Spectroscopy (XPS) was carried out on a ESCALAB 250Xi XPS system equipped with a monochromatic Al(K_α) X-ray source and a concentric hemispherical analyser. All XPS spectra were calibrated according to the position of the C *1*s peak. Field-emission scanning electron microscopy (FESEM) images were obtained on a Hitachi S-4200 SEM. Transmission electron microscopy (TEM) images were obtained on a Tecnai G220 TEM. The specific surface area of the *as*-prepared catalysts was calculated using the Brunauer–Emmett–Teller (BET, Micromeritics ASAP 2020) equation.

2.5 Electrochemical measurements

The electrochemical properties of the *as*-prepared materials were studied on a CHI 660E electrochemical workstation. The experiments were performed in a three-electrode configuration comprising the 1 cm^2 OZCN samples, the active carbon (AC), the Hg/HgO in 3.0 M KOH as a working electrode (WE), a counter electrode (CE) and a reference electrode (RE), respectively. To prepare the WE, 80 wt. % of porous carbon, 10 wt. % acetylene black, and 10 wt. %

polytetrafluoroethylene were ultrasonically mixed in a solution containing distilled water and ethanol, and then dried. The obtained sticky mixture was roll-pressed into a thin sheet, cut into small pieces, and finally pressed onto the nickel foam current collector. The loading mass of the active material was approximately 2.0 $mg.cm^{-2}$. Cyclic voltammetry (CV) measurements were carried out in a three-electrode setup in 3 M KOH. Galvanostatic charge/discharge (GCD) and cycling tests were conducted in a two-electrode configuration in 3 M KOH using a LAND CT2001A battery measurement system. The energy density (E) and the power density (P) were calculated from the following equations[37] :

$$E = I \int \Delta V dt / m \qquad (1)$$

$$P = E / \Delta t \qquad (2)$$

where I, t, m, ΔV, and A represent the discharge current (mA), the discharge time (s), the total mass of active materials (g) and the potential window of the electrode (V) in that order.

The asymmetric supercapacitor was fabricated by combining OZCN and AC as a cathode and an anode in a 3M KOH electrolyte. The mass loadings of the cathode and anode were calculated by using equation (3):

$$m^+/m^- = C^- \times \Delta E^- / (C^+ \times \Delta E^+) \qquad (3)$$

In this study, the mass ratio of the cathode and the anode was set at 2.9:1.

3. Results and Discussion

A typical synthetic strategy for truncated rhombic dodecahedral zeolitic imidazolate framework-8 (TRD-ZIF-8) derived oxygen vacancies-rich ZnO/g-C_3N_4 (OZCN) nanocomposites is schematically described in Scheme 1. Firstly, highly monodisperse sub-micrometer-sized colloidal TRD-ZIF-8 particles in water were fabricated and stabilized by using cetyltrimethylammonium bromide (CTAB) as a cationic surfactant and a capping agent. Subsequently, the obtained TRD-ZIF-8 powders were mixed with melamine by mechanical stirring, and then the mixture was calcined at 550 °C for 3 hours under aerobic conditions. During the heat-treatment process, g-C_3N_4 was produced and coated onto the surface of TRD-ZIF-8, whilst TRD-ZIF-8 was gradually decomposed and zinc ions were reduced into ZnO nanoparticles. After cooling down to room temperature, the characteristic yellowish of OZCN was obtained, in which TRD-ZIF-8 was transferred to ZnO nanoparticles and g-C_3N_4 nanosheets were formed on their surfaces.

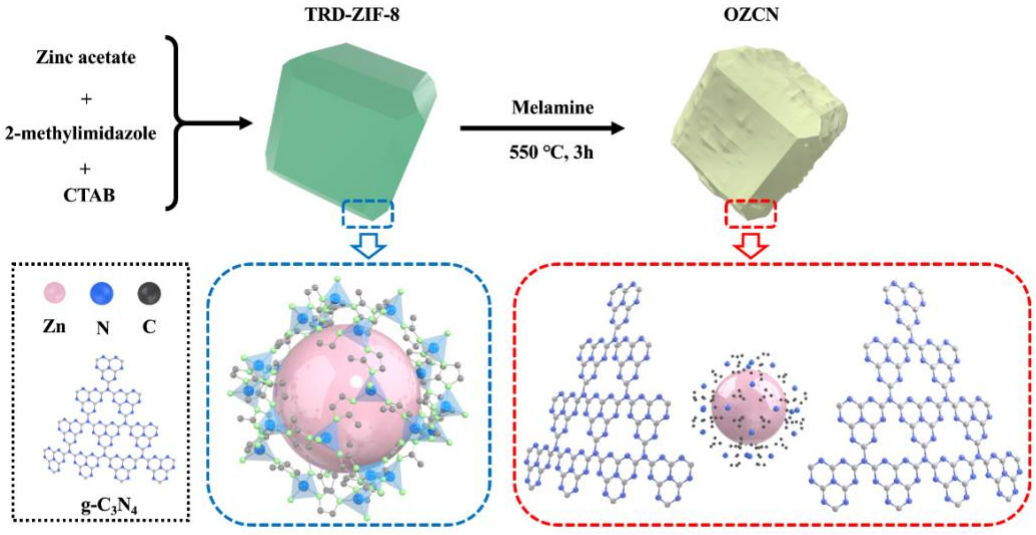

Scheme 1. Schematic diagram of formation of oxygen vacancies-rich ZnO/g-C_3N_4 (OZCN) nanocomposites.

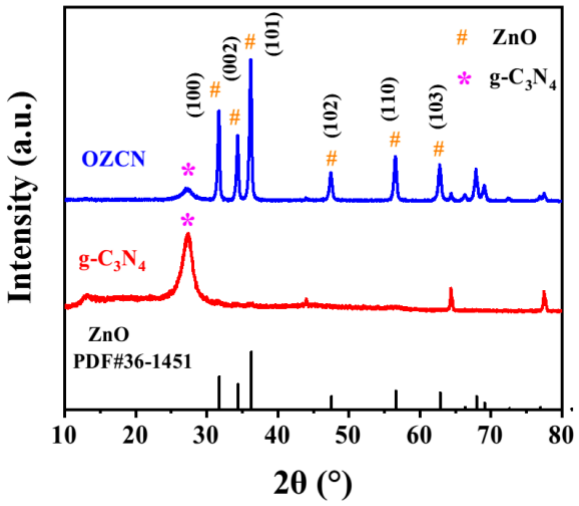

Figure 1. The XRD patterns of simulated ZnO powder, g-C_3N_4 and OZCN.

XRD patterns were firstly generated to examine the crystallographic feature of OZCN. On the XRD pattern of the *as*-formed OZCN, prominent *Bragg* reflections can be indexed as (100), (002), (101), (102), (110) and (103) planes of ZnO, respectively, which coincide with those of the simulated ZnO powder, indicating the synthesis of phase-pure crystalline ZnO nanoparticles (Figure 1). Moreover, the wide XRD peak appearing in the range of ca. 25 ° and 28 ° may be attributed to the layered g-C_3N_4 nanosheets[38]. More importantly, no obvious broad amorphous XRD peaks appeared for the OZCN material, indicating that TRD-ZIF-8 gradually decomposed into ZnO nanoparticles and carbon from small organic molecules could have been emitted as CO_2 during the calcination process under aerobic conditions. Moreover, the thermogravimetric analysis (TGA) under nitrogen (N_2) atmosphere was carried out to determine the carbon content in the OZCN nanocomposites. Figure S1 shows that the mass of OZCN remained unchanged (ca. 97.6 %) even under the 800 ℃ heating process, further confirming that a few carbon atoms were present in the OZCN nanocomposites.

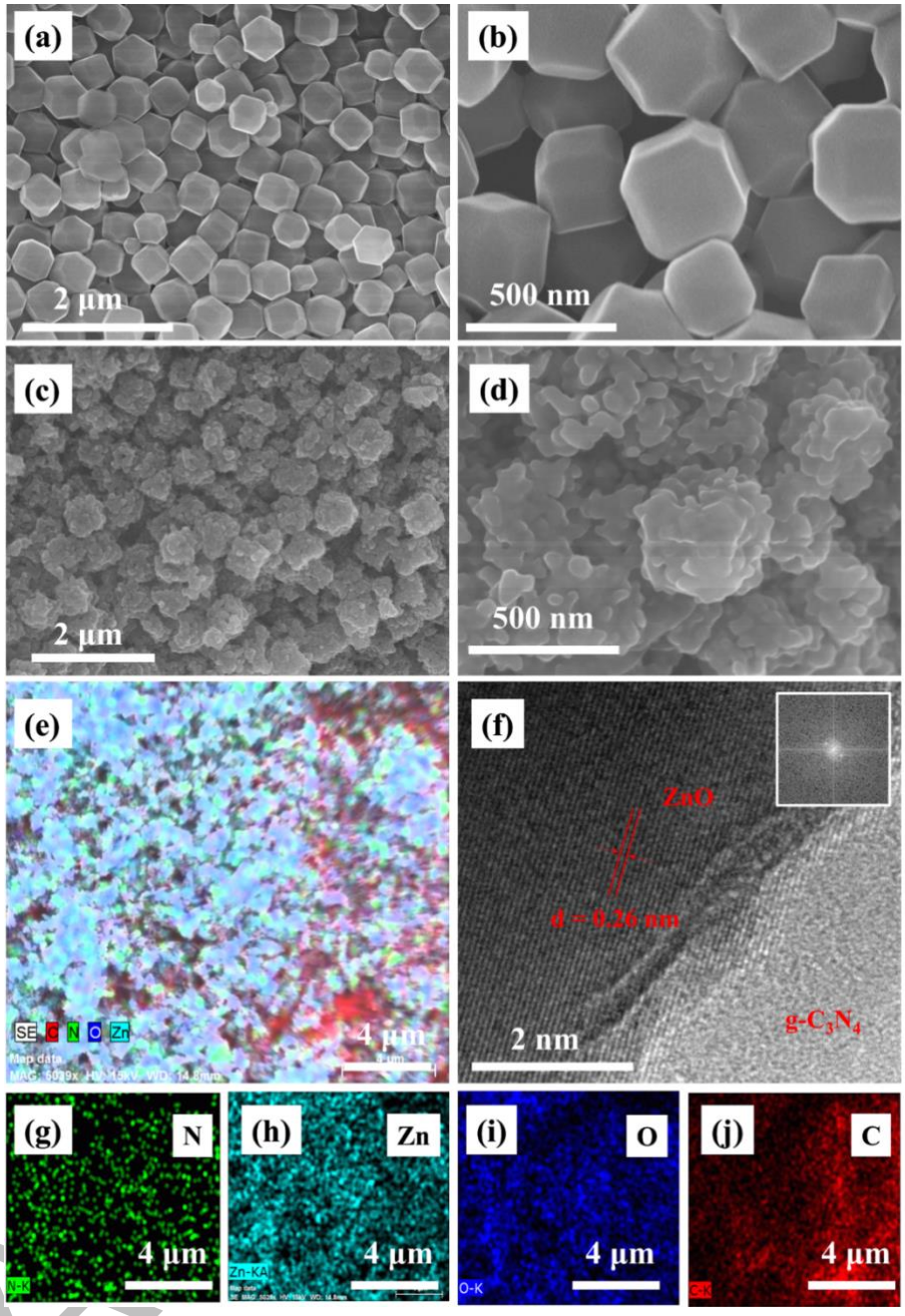

Figure 2. SEM and HR-SEM images of (a) (b) TRD-ZIF-8 and (c) (d) OZCN at different scale bars; (f) HRTEM image of OZCN and insert showing the crystal diffraction for ZnO nanoparticles; (e) SEM image of OZCN and corresponding elemental mapping images of (g) N, (h) Zn, (i) O and (j) C, respectively.

The morphology of the *as*-prepared TRD-ZIF-8 and OZCN materials were characterized by SEM images, as depicted in Figure 2. The figure shows that the TRD-

ZIF-8 nanoparticles are truncated rhombic dodecahedral crystals, and the particle size is approximately 210 ± 20 nm (Figure 2a and b). However, the SEM images of OZCN show a huge difference when compared to the precursor (Figure 2c and d). As shown in Figure 2c and 2d, the original nanostructure of TRD-ZIF-8 had been eliminated, and the smooth surface of TRD-ZIF-8 had changed to a rough surface after heating at high-temperature for 3 hours. High-resolved (HR) TEM images of OZCN show that OZCN nanocomposites were composed of ZnO nanoparticles and g-C_3N_4 nanosheets. The lattice diffraction shown in the insert figure of Figure 2f corresponds to the (101) planes of ZnO, and an interplanar spacing of ca. 0.26 nm of ZnO nanoparticle was observed. Moreover, it is clearly shown that g-C_3N_4 had been coated on the surface of ZnO, indicating that the rough surface on OZCN could be attributed to the formation of g-C_3N_4, due to the melamine acting as a "self-sacrificed template".

Figure S2 shows the EDAX pattern for OZCN. The EDAX spectrum elemental analysis was carried out to confirm the existence of C, Zn, O and N. The average atomic percentage of C: Zn :O: N is shown in the inset of Figure S2. It is worth mentioning that, according to the natural yellowish colour of the OZCN powder (Figure S3), this high carbon content may be due to the widespread presence of g-C_3N_4 on the surface of OZCN. The atomic percent data of Zn and O revealed the non-stoichiometric oxygen deficiency in ZnO, indicating the existence of oxygen vacancies (Vo) in the ZnO nanoparticles. Moreover, the mapping images of OZCN obtained from the low resolved SEM confirm the presence and distribution of C, O, Zn and N elements, and the presence of a g-C_3N_4 coated structure (Figure 2e and g-j).

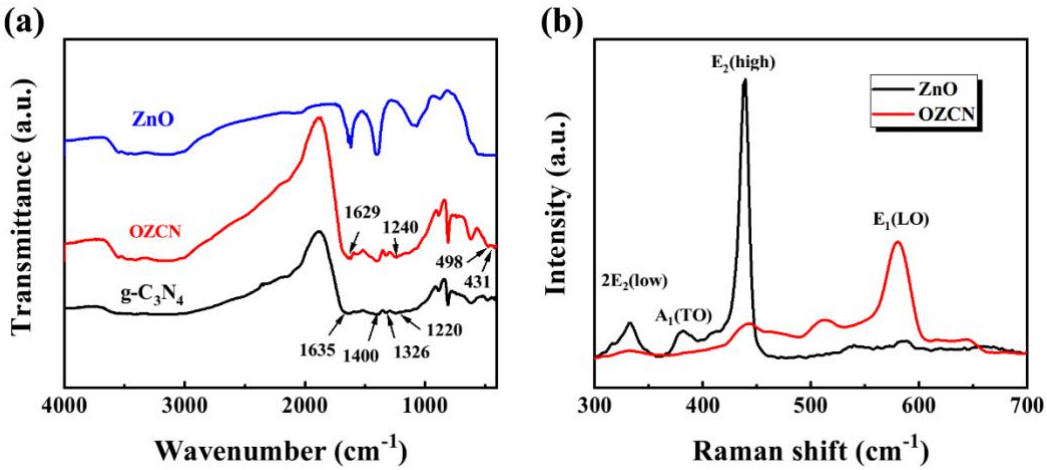

Figure 3. (a) FT-IR spectrum of commercial ZnO powder, g-C_3N_4 and OZCN; (b) Raman spectrum of commercial ZnO powder and OZCN.

The bond structure of OZCN nanocomposites was studied by FT-IR spectroscopy. Figure 3a shows the FT-IR spectra of commercial ZnO powder, pure g-C_3N_4 and OZCN. Several strong bands in the 1,200-1,650 cm^{-1} region of g-C_3N_4 and OZCN can be found, corresponding to the typical stretching modes of CN heterocycles. The peaks at ca. 1,635 and ca. 1,629 cm^{-1} can be attributed to the stretching vibration modes of heptazine-derived repeating units[39]. The peaks at ca. 1,326 and ca. 1,240 cm^{-1} may be assigned to the stretching vibrations of connected trigonal units of C-N(C)-C or the bridging C-NH-C (partial condensation)[40]. Moreover, compared to g-C_3N_4, the peaks at C=N bond (ca. 1,629 cm^{-1}) and C-N bonds (ca. 1,240 cm^{-1}) [41] of OZCN show a shift (in red), indicating the existence of a strong interaction between g-C_3N_4 and ZnO rather than a simple physical adsorption. The peak at ca. 814 cm^{-1} can be related to the tri-s-triazine ring modes[42]. It can be observed that the characteristic band of wurtzite ZnO is between ca. 600 and 400 cm^{-1}. Moreover, peaks of ca. 431 cm^{-1} and 498 cm^{-1} can be related to the oxygen non-stoichiometry of the materials[43]. Specifically, the peak at ca. 431 cm^{-1} can be ascribed to the Zn–O tensile vibration of hexagonal ZnO, and the peak

at 498 cm^{-1} is related to the composites with Vo[44], indicating the existence of oxygen defects/vacancies in ZnO of OZCN nanocomposites.

The BET surface area (SBET) of the OZCN was calculated by the N_2 adsorption-desorption measurement. As shown in Figure S4, the N_2 adsorption-desorption isotherms of the OZCN can be classified as type IV in the *IUPAC classification* suggesting the presence of micropores, which is in good agreement with the TEM results (Figure 2f). No obvious hysteresis loop in the pressure range ($0.1 < P/P_0 < 0.9$) associated with the intra-aggregated pores was observed, indicating that no large pores existed in the nanocomposites. Moreover, the pore size distribution curves obtained from the analysis of the desorption branch of the isotherms (REPHRASE). Table S1 lists the textural properties of bare OZCN. The specific surface areas of bare TRD-ZIF-8 and OZCN were found to be 953 $m^2.g^{-1}$ and only 8.59 $m^2\ g^{-1}$, respectively, indicating that the precursors (TRD-ZIF-8) was completely decomposed and the generated carbon was removed from the material[36].

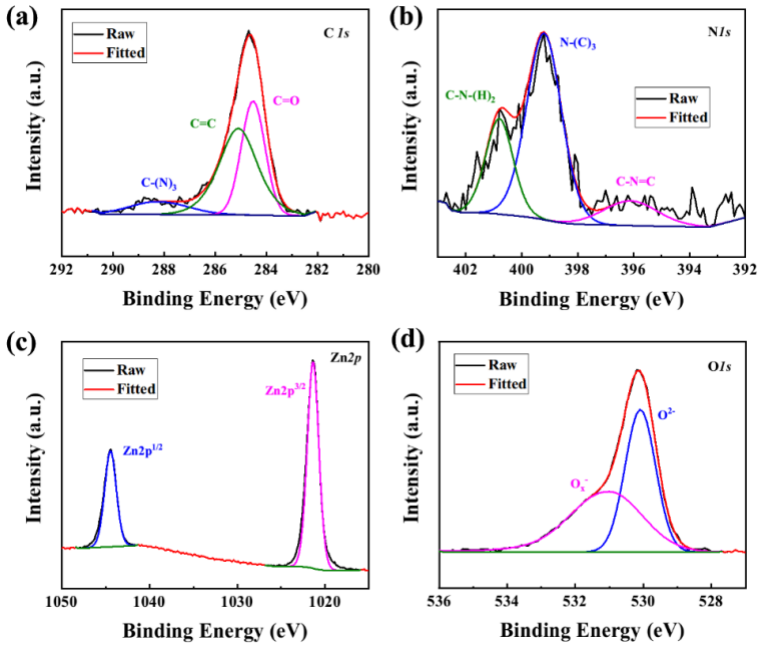

Figure 4. High-resolution (a) C*1s*, (b) N*1s*, (c) Zn*2p* and (d) O*1s* XPS spectra of OZCN.

XPS was used to investigate the valence states and chemical environment of constituent elements on the surface of the OZCN nanocomposites. The XPS survey spectrum in Figure S5 shows that the nanocomposites included carbon (C), nitrogen (N), oxygen (O) and zinc (Zn) elements. As depicted in Figure 4a, the primary peaks at ca. 284.5 eV and 285.2 eV are ascribed to the C=O and C=C components of the atmosphere, respectively[45]. Moreover, the peak at ca. 299.1 eV corresponds to C-$(N)_3$ binding energy of g-C_3N_4. Moreover, no peak appeared at ca. 282 eV, indicating that there was no direct bonding between C and Zn (C–Zn) in the nanocomposites[46], and all Zn atoms existed in the ZnO nanoparticles. The N *1s* region can be divided into three (3) energies (Figure 4b), which can be ascribed to C-N=C (ca. 396.1 eV), N-$(C)_3$ (ca. 399.2 eV) and C-N-$(H)_2$ groups (ca. 400.9 eV), respectively[47]. Figure 4c shows two symmetric peaks in the Zn *2p* region. The peak centered at ca. 1,021.3 eV corresponds to Zn $2p_{3/2}$ and the peak at ca. 1,044.6 eV may be attributed to Zn $2p_{1/2}$, respectively, which indicates a normal state of Zn *2p* in the ZnO[48]. Moreover, the binding energy gap between the two spin orbit interactions (Zn $2p_{3/2}$ and Zn $2p_{1/2}$) is ca. 23.1 eV, a value which is in very good agreement with previous reports[49]. Figure 4d shows the high-resolution O *1s* spectra of the OZCN. The two species centered at the banding energies of ca. 530.1 eV and 531.1 eV can be associated to the lattice oxygen anions (O^{2-}) in würzite structure, and the O_x^- ions (mainly O_2^-) in the oxygen-defective regions caused by Vo on the surface, respectively[39]. The ratios of O_x^- ions on the surface of OZCN was found to be ca. 50.93%, a value much higher than the reported ZnO-based composite (12.4%)[50], indicating that the OZCN has a high Vo concentration (Table S2).

Raman technique was further employed to identify the oxygen-defective nature of the *as*-prepared OZCN nanocomposites using commercial ZnO powder as a reference (Figure 3b). The Raman spectra indicated that the E1(LO) modes (located at ca. 582

cm^{-1}) of OZCN exhibited a much higher intensity compared to ZnO powder, which were generally assigned to the oxygen deficiencies such as Vo in ZnO in OZCN[51].

From the results, we concluded that the formation of oxygen vacancies rich ZnO in OZCN was a possible mechanism. According to the reported literature[52], Vo can be formed in the ZnO nanoparticles at high temperatures, even under aerobic conditions, which may be attributed to the low formation energy of Vo in ZnO[53]. In our conditions, the long-time high temperature calcination (ca. 550 ^{o}C) might have resulted in the oxygen-deficient atmosphere, which could have caused to the lattice oxygen moving to the interstitial positions, thereby generating Vo based on the defect equilibrium[18, 52] as follows:

$$ZnO \xrightarrow{\Delta} Vo + Zn_{Zn} + 1/2\ O_2 \quad (4)$$

$$1/2\ O_2 \longrightarrow O_{int} \quad (5)$$

where Vo represents the oxygen vacancy of the lattice site, Zn_{Zn} represents the lattice zinc, and O_{int} represents the interstitial oxygen. At high temperature, the interstitial oxygen gradually becomes unstable and diffuses out of the nanoparticles in the gas phase according to the following process:

$$2O_{int} \xrightarrow{\Delta} O_2(g) \quad (6)$$

Therefore, ZnO nanoparticles in OZCN will be generated with mass of Vo at high temperatures.

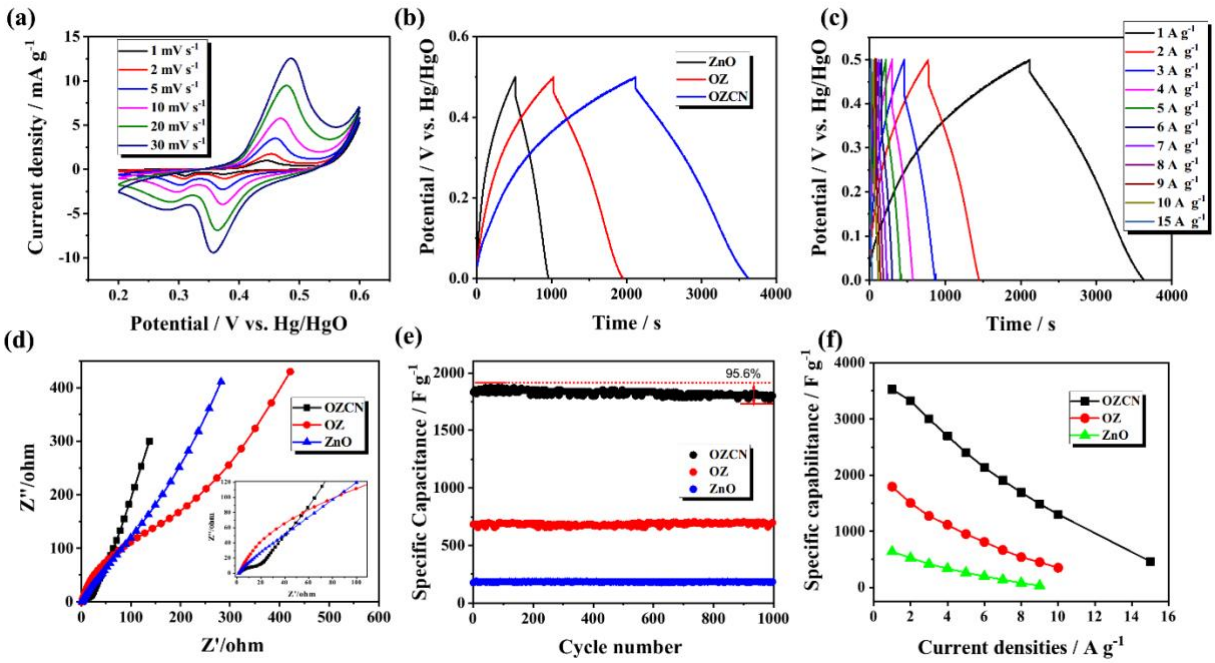

Figure 5. (a) CV curves of OZCN at various scan rates; (b) GCD curves of ZnO, OZ and OZCN at 1 A g^{-1}; (c) GCD curves of OZCN scanned at various current densities; (d) Nyquist plots of ZnO, OZ and OZCN; (e) cycling stability of ZnO, OZ and OZCN at the current density of 7 A g^{-1}; (f) specific capacitance of OZCN, OZ and ZnO scanned at various current densities.

Supercapacitive properties of OZCN were firstly examined by cyclic voltammetry (CV), galvanostatic charge-discharge (GCD) and electrochemical impedance spectroscopy (EIS) tests in a 3 M KOH aqueous electrolyte in a three-electrode system (Figure 5). From figure S6, it can be observed that the CV curves and redox peaks of OZCN are similar to those of the commercial ZnO powder, indicating that the oxygen vacancies-rich ZnO in OZCN plays an important role in the electrochemical process. Figure 5a shows the CV curves of the OZCN composite electrodes at different scan rates in the potential range +0.2 - +0.6 V *vs.* Hg/HgO. Redox peaks at ca. +0.35 V *vs.* Hg/HgO and +0.46 V *vs.* Hg/HgO were observed for all CV curves, indicating typical *pseudo-*

capacitive behaviour. It can be assumed that, during the *Faradaic* redox process, the intercalation and deintercalation of the alkali metal K^+ occurring on the electrode surface can be represented as follows:

$$ZnO + K^+ + e^- \leftrightarrow ZnOK \quad (7)$$

This process can be described as the electrochemical adsorption of anions on the surface of the electrode with rapid and reversible electron and the electrolyte. Moreover, it may be noted that the current in the CV curves increase linearly with increasing scan rates without any distortion of the CV shapes, due to the fast electron and ion transfer kinetics. The high current response from the OZCN electrode manifested itself by the same symmetrical redox peaks at different scan rates (Figure S7), indicating that the electrode material has outstanding rate capacity and relatively small interfacial resistance.

Capacities of OZCN, OZ and commercial ZnO materials were evaluated by GCD as shown in Figure 5b. The well-defined charge and discharge plateaus indicate *Faradaic* properties of OZCN, and the discharge time of OZCN is 2 times larger than that of OZ and even 3 times than that of ZnO, indicating its potentially excellent electrochemical performance. The GCD curves and corresponding specific capacitances for commercial ZnO, OZ and OZCN electrodes at various current densities are shown in Figures 5c and 5f. The specific capacitances for OZCN electrodes were found to be 3,528 $F.g^{-1}$ at $1A.g^{-1}$, 2,400 $F.g^{-1}$ at 5 $A.g^{-1}$ and 1,302 $F.g^{-1}$ at 10 A g^{-1}, respectively (Figure 5f); values that are much higher than those of pure g-C_3N_4, their composites and ZIF-8 derived composites (Table S3) [54-62]. Comparing OZ samples without the g-C_3N_4 component, OZCN electrodes exhibited superior capacitance ability, which might be due to the presence of g-C_3N_4. Moreover, OZ and OZCN materials showed much higher specific capacitance values than those of commercial ZnO, which could be attributed to the contribution of Vo mass on the surface of ZnO nanoparticles. The specific capacitance

of the OZCN electrode still remained as high as 465 $F.g^{-1}$ even at a high current density of 15 $A.g^{-1}$, which remained at 13.1% compared to that at 1$A.g^{-1}$. Furthermore, with the increase of current density, the specific capacitance showed a linear decrease without sudden or even sharp decline, which might be attributed to the electrode resistance and the insufficient Faradaic redox reaction of active materials, indicating that the electrode material is resistant under high current densities (> 10 $A.g^{-1}$). This finding suggests the material potential application as supercapacitor component under high currents.

The cycling stability at 7 $A.g^{-1}$ of the OZCN, OZ and commercial ZnO is also shown in Figure 5e. It was found that the lowest capacitance was observed for the bare ZnO (195 $F.g^{-1}$) and the highest capacitance for the OZCN (1,848 $F.g^{-1}$). Moreover, the OZCN electrode showed a 4.4% loss of its initial specific capacitance at 7 $A.g^{-1}$ after 1,000 charge-discharge cycles, indicating small degradation and thus excellent cycling stability of OZCN[63]

To further investigate the electrochemical behaviour of the OZCN material, EIS plots of OZCN, OZ and ZnO were generated and are shown in Figure 5d. In these plots, the low-frequency behaviour is important for a supercapacitor and the straight line, known as the Warburg resistance (W), is due to ion transport/diffusion of the electrolyte in the electrode. In the low frequency region, the slope of the straight-line region of EIS line for OZCN was maximum compared to other samples, indicating its low ion diffusion resistance, which in turns can result in faster Faradaic charge transfer during the electrochemical process. These results suggest that the synergetic effect of oxygen vacancies-rich ZnO and the conductivity of g-C_3N_4 enhances the electrochemical kinetics e.g. ion diffusion resistance. The reinforced properties of the composite materials can be explained as follows: (i) the introduction of g-C_3N_4 improves stability and electrical conductivity during the discharge-charge process, resulting in improved

rate performance, and (ii) high Vo content leads to highly improved conductivity and carrier transmission of ZnO, in turns yielding high specific capacitance values.

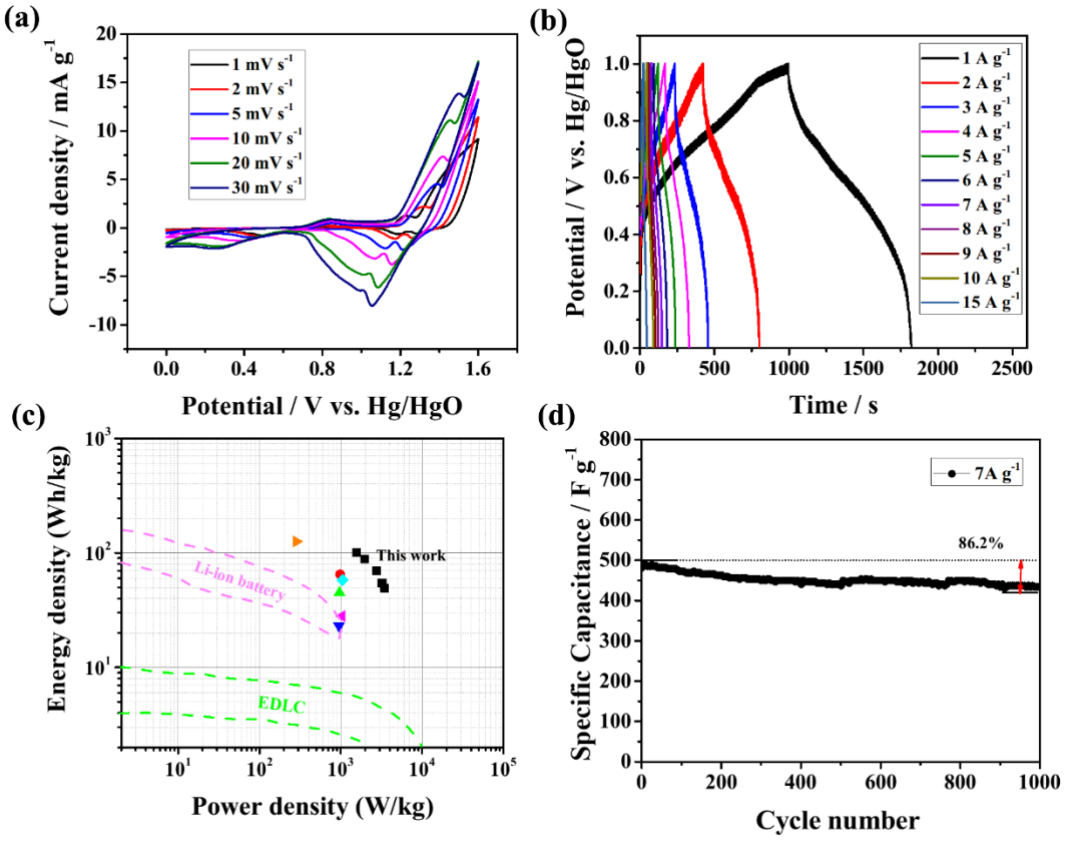

Figure 6. (a) CV curves at different scan rates and (b) GCD curves of OZCN at different current densities; (c) Ragone plot of as-assembled ASC and a comparison with the fields of EDLC, Li-ion batteries, and references; (d) cycling performance at 7 $A.g^{-1}$ under the measurements of ASC.

The performance of OZCN was evaluated under "real-world" conditions in a specially designed asymmetric supercapacitor (ACS). OZCN was employed as a positive electrode and commercial activated carbon (AC) as a negative electrode in 3M KOH as electrolyte; the mass ratio of the two electrodes was estimated to be 0.34 (*m*(OZCN)/*m*(AC)) in the asymmetric supercapacitors (OZCN//AS ASC).

CV curves of OZCN//AS ASC in the voltage window of 0-1.6 V at various current densities are shown in Figure 6a. The curves present large current areas with pairs of broad redox peaks, suggesting asymmetric *pseudo*-capacitor characteristic features consisting of battery-type and electrical double-layer electrode behaviour. Moreover, no obvious distortion of the CV shape was found when the current density increased from 1 to 30 $mV.s^{-1}$, demonstrating very fast and stable charge-discharge performance of OZCN//AS ASC. According to the discharge curves in the voltage range of 0-1V (Figure 6b), the capacitance of OZCN//AS ASC reached 840 $F.g^{-1}$ at 1 $A.g^{-1}$, as shown in Figure S8. With increasing current density, the specific capacitance decreased gradually due to the migration of the electrolyte ion was bound at high current densities. Figure 6d shows the cycling performance of OZCN//AS ASC at a current density of 7 $A.g^{-1}$for 1,000 cycles. After undergoing 1,000 cycles, the capacitance of the cells remained at ca. 86.2%, indicating that the asymmetric supercapacitor had excellent long-term stability. Compared with some reported literatures on g-C_3N_4 composites and ZIF-8 derived nanomaterials[64-66], it is clearly obvious that OZCN nanocomposites represent superior performance on specific capacitance together with low concentration electrolyte requirement, long-term stability and retention at high current densities.

The relationship between energy density and power density of OZCN//AS ASC was derived from the equations listed in the experimental section, and the corresponding Ragone plot is shown in Figure 6c. A high energy density of ca. 100.9 $Wh.kg^{-1}$ was obtained at ca. 1,572 $W.kg^{-1}$. When the power density increased to ca. 3,466 $W.kg^{-1}$, the energy density remained at ca. 49 $Wh.kg^{-1}$. Figure S9 shows the the EIS plot of OZCN//AS ASC with the fitted equivalent circuit. It can be observed that the solution resistance (R_s) of OZCN//AS ASC was found to be only 0.8 Ω and the transfer resistance (R_{ct}) was relatively low, indicating that high electrical conductivity of both

the electrodes and electrolyte, yielded in the excellent performance of OZCN//AS ASC. Two OZCN//AS ASC were connected in series to power a 3.0 V red LED light, as shown in Figure 7. It was observed that the LED light could be brightly light for more than 3 min, indicating the outstanding capacitance and stability of OZCN//AS ASC. In general, these results suggested that OZCN based supercapacitors offer advantages, such as low cost, high capacity, long-term stability and good rate capability, which can be used as a promising candidate for practical applications in electrochemical energy storage.

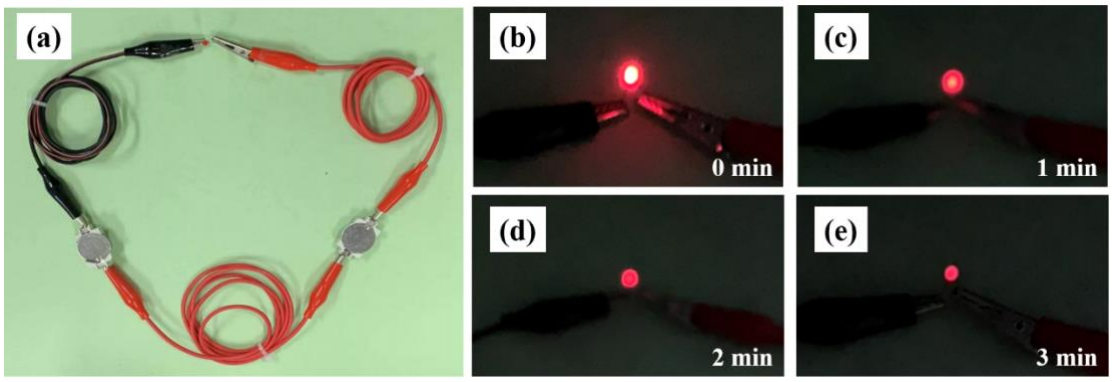

Figure 7. (a) Red LED light powered by two OZCN//AS ASC connected in series, and (b-e) corresponding the images of lighting time from 0 min - 3 min.

4. Conclusions

In this study, it was shown that we have successfully constructed a novel asymmetric supercapacitor in which a novel graphitic carbon nitride (g-C_3N_4) coated with oxygen vacancies-rich ZnO (OZCN) nanocomposites and activate carbon (AC) materials were used as positive and negative electrodes, respectively. The asymmetric supercapacitor (OZCN//AS ASC) exhibited a high specific capacitance and a stable cycling life. Moreover, the energy density and power density were found to be as high as 49 $Wh.kg^{-1}$ and 3,466 $W.kg^{-1}$, respectively. This outstanding performance was attributed to the contribution of the conductive g-C_3N_4 and oxygen vacancies-rich ZnO in OZCN, which improved ion exchange rate and carrier concentration, resulting in the enhancement of the electrochemical performance during discharge-charge process. This method offers an effective alternative approach to prepare g-C_3N_4-based oxygen vacancies-rich transition metal oxide composites as high-performance electrode materials for supercapacitors.

Acknowledgments

We would like to thank the financial support from National Natural Science Foundation of China (51661008 and 21766032), the Zhejiang Provincial Natural Science Foundation of China (LQ19F040005), Jiaxing Public Welfare Research Program (2018AY11007) and Jiaxing University SRT project (CD8517193136).

References

1. Zhang, L. L.; Zhao, X. S., Carbon-based materials as supercapacitor electrodes. *Chem. Soc. Rev.* 2009, *38* (9), 2520-2531.

2. Snook, G. A.; Kao, P.; Best, A. S., Conducting-polymer-based supercapacitor devices and electrodes. *J. Power Sources* 2011, *196* (1), 1-12.

3. Frackowiak, E., Carbon materials for supercapacitor application. *Phys. Chem. Chem. Phys.* 2007, *9* (15), 1774-1785.

4. Pan, H.; Li, J.; Feng, Y., Carbon Nanotubes for Supercapacitor. *Nanoscale Research Letters* 2010, *5* (3), 654.

5. Zhang, K.; Zhang, L. L.; Zhao, X. S.; Wu, J., Graphene/Polyaniline Nanofiber Composites as Supercapacitor Electrodes. *Chem. Mater.* 2010, *22* (4), 1392-1401.

6. Conway, B. E., Transition from "Supercapacitor" to "Battery" Behavior in Electrochemical Energy Storage. *J. Electrochem. Soc.* 1991, *138* (6), 1539-1548.

7. Zhang, Y.; Li, H.; Pan, L.; Lu, T.; Sun, Z., Capacitive behavior of graphene–ZnO composite film for supercapacitors. *J. Electroanal. Chem.* 2009, *634* (1), 68-71.

8. Yang, P.; Xiao, X.; Li, Y.; Ding, Y.; Qiang, P.; Tan, X.; Mai, W.; Lin, Z.; Wu, W.; Li, T.; Jin, H.; Liu, P.; Zhou, J.; Wong, C. P.; Wang, Z. L., Hydrogenated ZnO Core–Shell Nanocables for Flexible Supercapacitors and Self-Powered Systems. *ACS Nano* 2013, *7* (3), 2617-2626.

9. Lu, T.; Zhang, Y.; Li, H.; Pan, L.; Li, Y.; Sun, Z., Electrochemical behaviors of graphene–ZnO and graphene–SnO2 composite films for supercapacitors. *Electrochim.*

Acta 2010, *55* (13), 4170-4173.

10. Xing, Z.; Chu, Q.; Ren, X.; Ge, C.; Qusti, A. H.; Asiri, A. M.; Al-Youbi, A. O.; Sun, X., Ni3S2 coated ZnO array for high-performance supercapacitors. *J. Power Sources* 2014, *245*, 463-467.

11. Zhang, Y.; Sun, X.; Pan, L.; Li, H.; Sun, Z.; Sun, C.; Tay, B. K., Carbon nanotube–ZnO nanocomposite electrodes for supercapacitors. *Solid State Ionics* 2009, *180* (32), 1525-1528.

12. Selvakumar, M.; Krishna Bhat, D.; Manish Aggarwal, A.; Prahladh Iyer, S.; Sravani, G., Nano ZnO-activated carbon composite electrodes for supercapacitors. *Physica B: Condensed Matter* 2010, *405* (9), 2286-2289.

13. Li, G.-R.; Wang, Z.-L.; Zheng, F.-L.; Ou, Y.-N.; Tong, Y.-X., ZnO@MoO3 core/shell nanocables: facile electrochemical synthesis and enhanced supercapacitor performances. *J. Mater. Chem.* 2011, *21* (12), 4217-4221.

14. Kim, C. H.; Kim, B.-H., Zinc oxide/activated carbon nanofiber composites for high-performance supercapacitor electrodes. *J. Power Sources* 2015, *274*, 512-520.

15. Zhang, Y.; Sun, X.; Pan, L.; Li, H.; Sun, Z.; Sun, C.; Tay, B. K., Carbon nanotube–zinc oxide electrode and gel polymer electrolyte for electrochemical supercapacitors. *J. Alloys Compd.* 2009, *480* (2), L17-L19.

16. Zilong, W.; Zhu, Z.; Qiu, J.; Yang, S., High performance flexible solid-state asymmetric supercapacitors from MnO2/ZnO core–shell nanorods//specially reduced graphene oxide. *Journal of Materials Chemistry C* 2014, *2* (7), 1331-1336.

17. Chee, W. K.; Lim, H. N.; Harrison, I.; Chong, K. F.; Zainal, Z.; Ng, C. H.; Huang,

N. M., Performance of Flexible and Binderless Polypyrrole/Graphene Oxide/Zinc Oxide Supercapacitor Electrode in a Symmetrical Two-Electrode Configuration. *Electrochim. Acta* 2015, *157*, 88-94.

18. Dillip, G. R.; Banerjee, A. N.; Anitha, V. C.; Deva Prasad Raju, B.; Joo, S. W.; Min, B. K., Oxygen Vacancy-Induced Structural, Optical, and Enhanced Supercapacitive Performance of Zinc Oxide Anchored Graphitic Carbon Nanofiber Hybrid Electrodes. *ACS Appl. Mater. Interfaces* 2016, *8* (7), 5025-5039.

19. Yan, D.; Wang, W.; Luo, X.; Chen, C.; Zeng, Y.; Zhu, Z., NiCo2O4 with oxygen vacancies as better performance electrode material for supercapacitor. *Chem. Eng. J.* 2018, *334*, 864-872.

20. Zhai, T.; Xie, S.; Yu, M.; Fang, P.; Liang, C.; Lu, X.; Tong, Y., Oxygen vacancies enhancing capacitive properties of MnO2 nanorods for wearable asymmetric supercapacitors. *Nano Energy* 2014, *8*, 255-263.

21. Wang, J.; Chen, R.; Xiang, L.; Komarneni, S., Synthesis, properties and applications of ZnO nanomaterials with oxygen vacancies: A review. *Ceram. Int.* 2018, *44* (7), 7357-7377.

22. Gurav, K. V.; Gang, M. G.; Shin, S. W.; Patil, U. M.; Deshmukh, P. R.; Agawane, G. L.; Suryawanshi, M. P.; Pawar, S. M.; Patil, P. S.; Lokhande, C. D.; Kim, J. H., Gas sensing properties of hydrothermally grown ZnO nanorods with different aspect ratios. *Sensors and Actuators B: Chemical* 2014, *190*, 439-445.

23. Kalpana, D.; Omkumar, K. S.; Kumar, S. S.; Renganathan, N. G., A novel high power symmetric ZnO/carbon aerogel composite electrode for electrochemical

supercapacitor. *Electrochim. Acta* 2006, *52* (3), 1309-1315.

24. Baek, M.; Kim, D.; Yong, K., Simple but Effective Way To Enhance Photoelectrochemical Solar-Water-Splitting Performance of ZnO Nanorod Arrays: Charge-Trapping Zn(OH)2 Annihilation and Oxygen Vacancy Generation by Vacuum Annealing. *ACS Appl. Mater. Interfaces* 2017, *9* (3), 2317-2325.

25. Fang, L.; Zhang, B.; Li, W.; Zhang, J.; Huang, K.; Zhang, Q., Fabrication of highly dispersed ZnO nanoparticles embedded in graphene nanosheets for high performance supercapacitors. *Electrochim. Acta* 2014, *148*, 164-169.

26. Xu, Y.; Zhou, Y.; Guo, J.; Zhang, S.; Lu, Y., Preparation of the poly (3,4-ethylenedioxythiophene):poly(styrenesulfonate)@g-C3N4 composite by a simple direct mixing method for supercapacitor. *Electrochim. Acta* 2018, *283*, 1468-1474.

27. Guo, W.; Ming, S.; Chen, Z.; Bi, J.; Ma, Y.; Wang, J.; Li, T., A Novel CVD Growth of g-C3N4 Ultrathin Film on NiCo2O4 Nanoneedles/Carbon Cloth as Integrated Electrodes for Supercapacitors. *ChemElectroChem* 2018, *5* (22), 3383-3390.

28. Chen, A. Y.; Zhang, T. T.; Qiu, Y. J.; Wang, D.; Wang, P.; Li, H. J.; Li, Y.; Yang, J. H.; Wang, X. Y.; Xie, X. F., Construction of nanoporous gold/g-C3N4 heterostructure for electrochemical supercapacitor. *Electrochim. Acta* 2019, *294*, 260-267.

29. Dong, B.; Li, M.; Chen, S.; Ding, D.; Wei, W.; Gao, G.; Ding, S., Formation of g-C3N4@Ni(OH)2 Honeycomb Nanostructure and Asymmetric Supercapacitor with High Energy and Power Density. *ACS Appl. Mater. Interfaces* 2017, *9* (21), 17890-17896.

30. Palanivel, B.; Mudisoodum perumal, S. d.; Maiyalagan, T.; Jayarman, V.; Ayyappan, C.; Alagiri, M., Rational design of ZnFe2O4/g-C3N4 nanocomposite for enhanced photo-Fenton reaction and supercapacitor performance. *Appl. Surf. Sci.* 2019, *498*, 143807.

31. Ouyang, Y.; Xia, X.; Ye, H.; Wang, L.; Jiao, X.; Lei, W.; Hao, Q., Three-Dimensional Hierarchical Structure ZnO@C@NiO on Carbon Cloth for Asymmetric Supercapacitor with Enhanced Cycle Stability. *ACS Appl. Mater. Interfaces* 2018, *10* (4), 3549-3561.

32. Chen, X.; Zhu, X.; Xiao, Y.; Yang, X., PEDOT/g-C3N4 binary electrode material for supercapacitors. *J. Electroanal. Chem.* 2015, *743*, 99-104.

33. Tang, L.; Jia, C.-t.; Xue, Y.-c.; Li, L.; Wang, A.-q.; Xu, G.; Liu, N.; Wu, M.-h., Fabrication of compressible and recyclable macroscopic g-C3N4/GO aerogel hybrids for visible-light harvesting: A promising strategy for water remediation. *Applied Catalysis B: Environmental* 2017, *219*, 241-248.

34. Bu, Y.; Chen, Z., Highly efficient photoelectrochemical anticorrosion performance of C3N4@ZnO composite with quasi-shell–core structure on 304 stainless steel. *RSC Advances* 2014, *4* (85), 45397-45406.

35. Liu, C.; Qiu, Y.; Wang, F.; Wang, K.; Liang, Q.; Chen, Z., Design of Core–Shell-Structured ZnO/ZnS Hybridized with Graphite-Like C3N4 for Highly Efficient Photoelectrochemical Water Splitting. *Adv. Mater. Interfaces* 2017, *4* (21), 1700681.

36. Avci, C.; Imaz, I.; Carné-Sánchez, A.; Pariente, J. A.; Tasios, N.; Pérez-Carvajal, J.; Alonso, M. I.; Blanco, A.; Dijkstra, M.; López, C.; Maspoch, D., Self-assembly of

polyhedral metal–organic framework particles into three-dimensional ordered superstructures. *Nat. Chem.* 2018, *10* (1), 78-84.

37. Lin, J.; Zhong, Z.; Wang, H.; Zheng, X.; Wang, Y.; Qi, J.; Cao, J.; Fei, W.; Huang, Y.; Feng, J., Rational constructing free-standing Se doped nickel-cobalt sulfides nanotubes as battery-type electrode for high-performance supercapattery. *J. Power Sources* 2018, *407*, 6-13.

38. Wang, D.; Wang, Y.; Chen, Y.; Liu, W.; Wang, H.; Zhao, P.; Li, Y.; Zhang, J.; Dong, Y.; Hu, S.; Yang, J., Coal tar pitch derived N-doped porous carbon nanosheets by the in-situ formed g-C3N4 as a template for supercapacitor electrodes. *Electrochim. Acta* 2018, *283*, 132-140.

39. Li, X.; Li, M.; Yang, J.; Li, X.; Hu, T.; Wang, J.; Sui, Y.; Wu, X.; Kong, L., Synergistic effect of efficient adsorption g-C3N4/ZnO composite for photocatalytic property. *J. Phys. Chem. Solids* 2014, *75* (3), 441-446.

40. Lotsch, B. V.; Döblinger, M.; Sehnert, J.; Seyfarth, L.; Senker, J.; Oeckler, O.; Schnick, W., Unmasking Melon by a Complementary Approach Employing Electron Diffraction, Solid-State NMR Spectroscopy, and Theoretical Calculations—Structural Characterization of a Carbon Nitride Polymer. *Chemistry–A European Journal* 2007, *13* (17), 4969-4980.

41. Wang, Y.; Wang, Z.; Muhammad, S.; He, J., Graphite-like C3N4 hybridized ZnWO4 nanorods: Synthesis and its enhanced photocatalysis in visible light. *CrystEngComm* 2012, *14* (15), 5065-5070.

42. Liu, J.; Zhang, T.; Wang, Z.; Dawson, G.; Chen, W., Simple pyrolysis of urea into

graphitic carbon nitride with recyclable adsorption and photocatalytic activity. *J. Mater. Chem.* 2011, *21* (38), 14398-14401.

43. Djelloul, A.; Aida, M. S.; Bougdira, J., Photoluminescence, FTIR and X-ray diffraction studies on undoped and Al-doped ZnO thin films grown on polycrystalline α-alumina substrates by ultrasonic spray pyrolysis. *J. Lumin.* 2010, *130* (11), 2113-2117.

44. Xiong, G.; Pal, U.; Serrano, J. G.; Ucer, K. B.; Williams, R. T., Photoluminesence and FTIR study of ZnO nanoparticles: the impurity and defect perspective. *physica status solidi c* 2006, *3* (10), 3577-3581.

45. Wei, B.; Liang, H.; Wang, R.; Zhang, D.; Qi, Z.; Wang, Z., One-step synthesis of graphitic-C3N4/ZnS composites for enhanced supercapacitor performance. *J. Energy Chem.* 2018, *27* (2), 472-477.

46. Samadi, M.; Shivaee, H. A.; Zanetti, M.; Pourjavadi, A.; Moshfegh, A., Visible light photocatalytic activity of novel MWCNT-doped ZnO electrospun nanofibers. *J. Mol. Catal. A: Chem.* 2012, *359*, 42-48.

47. Dong, B.; Li, M.; Chen, S.; Ding, D.; Wei, W.; Gao, G.; Ding, S., Formation of g-C3N4@ Ni (OH) 2 honeycomb nanostructure and asymmetric supercapacitor with high energy and power density. *ACS Appl. Mater. Interfaces* 2017, *9* (21), 17890-17896.

48. Sahu, V.; Goel, S.; Sharma, R. K.; Singh, G., Zinc oxide nanoring embedded lacey graphene nanoribbons in symmetric/asymmetric electrochemical capacitive energy storage. *Nanoscale* 2015, *7* (48), 20642-20651.

49. Zhou, J.-H.; Sui, Z.-J.; Zhu, J.; Li, P.; Chen, D.; Dai, Y.-C.; Yuan, W.-K., Characterization of surface oxygen complexes on carbon nanofibers by TPD, XPS and FT-IR. *Carbon* 2007, *45* (4), 785-796.

50. Wang, J.; Xia, Y.; Zhao, H.; Wang, G.; Xiang, L.; Xu, J.; Komarneni, S., Oxygen defects-mediated Z-scheme charge separation in g-C3N4/ZnO photocatalysts for enhanced visible-light degradation of 4-chlorophenol and hydrogen evolution. *Applied Catalysis B: Environmental* 2017, *206*, 406-416.

51. Özgür, Ü.; Alivov, Y. I.; Liu, C.; Teke, A.; Reshchikov, M. A.; Doğan, S.; Avrutin, V.; Cho, S.-J.; Morkoç, H., A comprehensive review of ZnO materials and devices. *J. Appl. Phys.* 2005, *98* (4), 041301.

52. Hai-Bo, F.; Shao-Yan, Y.; Pan-Feng, Z.; Hong-Yuan, W.; Xiang-Lin, L.; Chun-Mei, J.; Qin-Sheng, Z.; Yong-Hai, C.; Zhan-Guo, W., Investigation of Oxygen Vacancy and Interstitial Oxygen Defects in ZnO Films by Photoluminescence and X-Ray Photoelectron Spectroscopy. *Chin. Phys. Lett.* 2007, *24* (7), 2108-2111.

53. Van de Walle, C. G., Defect analysis and engineering in ZnO. *Physica B: Condensed Matter* 2001, *308-310*, 899-903.

54. Tahir, M.; Cao, C.; Butt, F. K.; Idrees, F.; Mahmood, N.; Ali, Z.; Aslam, I.; Tanveer, M.; Rizwan, M.; Mahmood, T., Tubular graphitic-C3N4: a prospective material for energy storage and green photocatalysis. *Journal of Materials Chemistry A* 2013, *1* (44), 13949-13955.

55. Tahir, M.; Cao, C.; Mahmood, N.; Butt, F. K.; Mahmood, A.; Idrees, F.; Hussain, S.; Tanveer, M.; Ali, Z.; Aslam, I., Multifunctional g-C3N4 Nanofibers: A Template-

Free Fabrication and Enhanced Optical, Electrochemical, and Photocatalyst Properties. *ACS Appl. Mater. Interfaces* 2014, *6* (2), 1258-1265.

56. Shi, L.; Zhang, J.; Liu, H.; Que, M.; Cai, X.; Tan, S.; Huang, L., Flower-like Ni(OH)2 hybridized g-C3N4 for high-performance supercapacitor electrode material. *Mater. Lett.* 2015, *145*, 150-153.

57. Wan, L.; Shamsaei, E.; Easton, C. D.; Yu, D.; Liang, Y.; Chen, X.; Abbasi, Z.; Akbari, A.; Zhang, X.; Wang, H. J. C., ZIF-8 derived nitrogen-doped porous carbon/carbon nanotube composite for high-performance supercapacitor. *Carbon* 2017, *121*, 330-336.

58. Liu, X.; Zhou, L.; Zhao, Y.; Bian, L.; Feng, X.; Pu, Q. J. A. a. m.; interfaces, Hollow, spherical nitrogen-rich porous carbon shells obtained from a porous organic framework for the supercapacitor. *ACS Appl. Mater. Interfaces* 2013, *5* (20), 10280-10287.

59. Zhong, S.; Zhan, C.; Cao, D. J. C., Zeolitic imidazolate framework-derived nitrogen-doped porous carbons as high performance supercapacitor electrode materials. *Carbon* 2015, *85*, 51-59.

60. Lai, F.; Miao, Y. E.; Zuo, L.; Lu, H.; Huang, Y.; Liu, T. J. S., Biomass-Derived Nitrogen-Doped Carbon Nanofiber Network: A Facile Template for Decoration of Ultrathin Nickel-Cobalt Layered Double Hydroxide Nanosheets as High-Performance Asymmetric Supercapacitor Electrode. *Small* 2016, *12* (24), 3235-3244.

61. Chen, X. Y.; He, Y. Y.; Song, H.; Zhang, Z. J. J. C., Structure and electrochemical performance of highly nanoporous carbons from benzoate–metal complexes by a

template carbonization method for supercapacitor application. *Carbon* 2014, *72*, 410-420.

62. Jiang, M.; Cao, X.; Zhu, D.; Duan, Y.; Zhang, J. J. E. A., Hierarchically porous N-doped carbon derived from ZIF-8 nanocomposites for electrochemical applications. *Electrochim. Acta* 2016, *196*, 699-707.

63. Wang, D.; Wang, Y.; Chen, Y.; Liu, W.; Wang, H.; Zhao, P.; Li, Y.; Zhang, J.; Dong, Y.; Hu, S., Coal tar pitch derived N-doped porous carbon nanosheets by the in-situ formed g-C3N4 as a template for supercapacitor electrodes. *Electrochim. Acta* 2018, *283*, 132-140.

64. Zhang, Y.; Li, H.; Pan, L.; Lu, T.; Sun, Z. J. J. o. E. C., Capacitive behavior of graphene–ZnO composite film for supercapacitors. *J. Electroanal. Chem.* 2009, *634* (1), 68-71.

65. Shayeh, J. S.; Salari, H.; Daliri, A.; Omidi, M. J. A. S. S., Decorative reduced graphene oxide/C3N4/Ag2O/conductive polymer as a high performance material for electrochemical capacitors. *Appl. Surf. Sci.* 2018, *447*, 374-380.

66. Zhao, Y.; Xu, L.; Huang, S.; Bao, J.; Qiu, J.; Lian, J.; Xu, L.; Huang, Y.; Xu, Y.; Li, H. J. J. o. A.; Compounds, Facile preparation of TiO2/C3N4 hybrid materials with enhanced capacitive properties for high performance supercapacitors. *J. Alloys Compd.* 2017, *702*, 178-185.